

See discussions, stats, and author profiles for this publication at: <https://www.researchgate.net/publication/5226784>

# Characterization and Application of Controllable Local Chemical Changes Produced by Reagent Delivery from a Nanopipet

ARTICLE in JOURNAL OF THE AMERICAN CHEMICAL SOCIETY · AUGUST 2008

Impact Factor: 12.11 · DOI: 10.1021/ja8022253 · Source: PubMed

---

CITATIONS

25

---

READS

44

7 AUTHORS, INCLUDING:



Chien-Jung Lo

National Central University

21 PUBLICATIONS 345 CITATIONS

SEE PROFILE



Liming Ying

Imperial College London

75 PUBLICATIONS 2,475 CITATIONS

SEE PROFILE

## Characterization and Application of Controllable Local Chemical Changes Produced by Reagent Delivery from a Nanopipet

Joe D. Piper,<sup>†</sup> Chao Li,<sup>†</sup> Chien-Jung Lo,<sup>‡</sup> Richard Berry,<sup>‡</sup> Yuri Korchev,<sup>§</sup>  
Liming Ying,<sup>||</sup> and David Klennerman<sup>\*,†</sup>

*Department of Chemistry, University of Cambridge, Lensfield Road, Cambridge CB2 1EW, U.K.,  
Department of Physics, Clarendon Laboratory, University of Oxford, Parks Road,  
Oxford OX1 3PU, U.K., MRC Clinical Science Centre, Division of Medicine, Imperial College  
London, London W12 0NN, U.K., and Molecular Medicine, National Heart and Lung Institute,  
Imperial College London, London SW7 2AZ, U.K.*

Received March 26, 2008; E-mail: dk10012@cam.ac.uk

**Abstract:** We introduce a versatile method that allows local and repeatable delivery (or depletion) of any water-soluble reagent from a nanopipet in ionic solution to make localized controlled changes in reagent concentration at a surface. In this work,  $\text{Na}^+$  or  $\text{OH}^-$  ions were dosed from the pipet using pulsed voltage-driven delivery. Total internal reflection fluorescence from CoroNa Green dye in the bath for  $\text{Na}^+$  ions or fluorescein in the bath for pH quantified the resulting changes in local surface concentration. These changes had a time response as short as 10 ms and a radius of 1–30  $\mu\text{m}$  and depended on the diameter of the pipet used, the applied voltage, and the pipet–surface separation. After the pipet dosing was characterized in detail, two proof-of-concept experiments on single cells and single molecules were then performed. We demonstrated local control of the sodium-sensitive flagellar motor in single *Escherichia coli* chimera on the time scale of 1 s by dosing sodium and monitoring the rotation of a 1  $\mu\text{m}$  diameter bead fixed to the flagellum. We also demonstrated triggered single-molecule unfolding by dosing acid from the pipet to locally melt individual molecules of duplex DNA, as observed using fluorescent resonance energy transfer.

### 1. Introduction

There is a general need to develop ways to produce local controllable chemical, biochemical, or cellular changes on the micro- to nanoscale. This could be used to initiate chemical or biochemical reactions at a surface under solution, which could then be followed temporally or used to modulate or initiate a cellular response. Repeating these experiments at different positions on the surface would produce a map of chemical or biochemical reactivity. Rapid initiation of reactions on surface-immobilized molecules would also be highly advantageous in the field of single-molecule biophysics for studies under nonequilibrium conditions. In order to perform such experiments, the ability to produce a local concentration change of known size at the surface is essential, since the concentration produced will determine the rate of any resulting chemical or biochemical reaction.

Microfluidics offer parallel manipulation but are limited in simultaneously generating stable chemical gradients while allowing fast concentration changes that can trigger reactions.<sup>1</sup> Careful engineering is required in order to combine sample preparation with precise introduction of species such as fluo-

rescent dyes.<sup>2</sup> Methods for generating concentration gradients have included the multipurpose microfluidic probe (MFP)<sup>3</sup> and engineered “microcanals” to allow micropipet access.<sup>4</sup> The MFP operates  $\sim 30 \mu\text{m}$  above the surface and offers impressive patterning of surfaces with diameters as small as  $\sim 20 \mu\text{m}$  within 300 ms.<sup>3</sup> It varies the dosed concentration through the speed of scanning, separation from the surface, and injection/aspiration flow rates.<sup>3</sup> Microperfusion is another established technique for changing a cell’s surroundings;<sup>5,6</sup> this has been combined with microfluidics for cell-based assays<sup>7</sup> or micropipets to hold robust individual cells,<sup>8</sup> but it lacks the ability to create localized changes in reaction conditions.

Scanning probe microscopy has the potential for local delivery of reagents to surfaces, as, for example, in the use of dip-pen nanolithography for deposition and removal.<sup>9–11</sup> Scanning electrochemical microscopy (SECM) can use ultramicroelec-

<sup>†</sup> University of Cambridge.

<sup>‡</sup> University of Oxford.

<sup>§</sup> MRC Clinical Science Centre, Imperial College London.

<sup>||</sup> National Heart and Lung Institute, Imperial College London.

(1) Irimia, D.; Liu, S. Y.; Tharp, W. G.; Samadani, A.; Toner, M.; Poznansky, M. C. *Lab Chip* **2006**, *6*, 191–198.

(2) Takayama, S.; Ostuni, E.; LeDuc, P.; Naruse, K.; Ingber, D. E.; Whitesides, G. M. *Nature* **2001**, *411*, 1016.

(3) Juncker, D.; Schmid, H.; Delamarche, E. *Nat. Mater.* **2005**, *4*, 622–628.

(4) Hsu, C. H.; Chen, C. C.; Folch, A. *Lab Chip* **2004**, *4*, 420–424.

(5) Poyton, R. O.; Branton, D. *Exp. Cell Res.* **1970**, *60*, 109–114.

(6) Gao, D. Y.; Benson, C. T.; Liu, C.; McGrath, J. J.; Critser, E. S.; Critser, J. K. *Biophys. J.* **1996**, *71*, 443–450.

(7) Hung, P. J.; Lee, P. J.; Sabounchi, P.; Lin, R.; Lee, L. P. *Biotechnol. Bioeng.* **2005**, *89*, 1–8.

(8) Gao, D. Y.; McGrath, J. J.; Tao, J.; Benson, C. T.; Critser, E. S.; Critser, J. K. *J. Reprod. Fertil.* **1994**, *102*, 385–392.

(9) Tinazli, A.; Piehler, J.; Beutler, M.; Guckenberger, R.; Tampe, R. *Nat. Nanotechnol.* **2007**, *2*, 220–225.

trodes to produce local pH changes<sup>12</sup> over a time scale of seconds.<sup>13</sup> However, the need for reagent replenishment and general methods for different analytes has guided research into hollow tips.<sup>14</sup> Pressure-based ejection (or “puffing”) from a 1–2  $\mu\text{m}$  diameter micropipet is frequently used to examine cell responses, particularly in electrophysiology.<sup>15,16</sup> Visualization of this technique by puffing an opaque dye (Procion Black) showed a dosing radius of  $\sim 50\ \mu\text{m}$  with a response time of 100 ms when close to the center that rose to 1 s when  $\sim 35\ \mu\text{m}$  away.<sup>17</sup> Longer puffs caused erratic dosing quantities and pipet clogging, so delivery times are restricted to  $\sim 40$  ms pulses with a pressure of 10–15 PSI.<sup>17</sup> The “puffer pipet” must be correctly oriented to ensure that the initial spray targets only the intended area of the cell while the residual cloud dissipates away.<sup>18</sup> Although an electrochemical attosyringe based on a nanopipet containing an immiscible liquid can locally sample and dispense, it lacks bulk storage capability<sup>19</sup> and hence cannot maintain a local concentration change for a prolonged period. These shortages, fluid-displacement effects, and localization can be improved by the use of nanopipets having large reagent reservoirs.<sup>20,21</sup>

Scanning ion conductance microscopy (SICM)<sup>22</sup> is a form of scanning probe microscopy that is based on nanopipets. SICM uses the ion current flowing through the pipet tip for robust noncontact imaging of living cells.<sup>23</sup> The nanopipet can also be used for voltage-driven deposition of biomolecules onto surfaces, and submicron-feature size has been demonstrated.<sup>21</sup> Voltage-driven delivery via electrophoresis is a less perturbative method than pressure ejection since there is no bulk flow of liquid. With respect to cells, the pipet has also been used for local delivery of  $\text{K}^+$  ions onto live cardiac myocytes. Here an increase in the whole cell current was detected when the pipet was over an ATP-dependent  $\text{K}^+$  ion channel, allowing the position and activity of these ion channels to be mapped.<sup>24</sup> In addition, delivery of  $\alpha$  toxins<sup>25</sup> and individual labeled proteins onto cell membranes has been demonstrated.<sup>26</sup> The pipet has also been used as a nanosensor that traps ion-selective fluores-

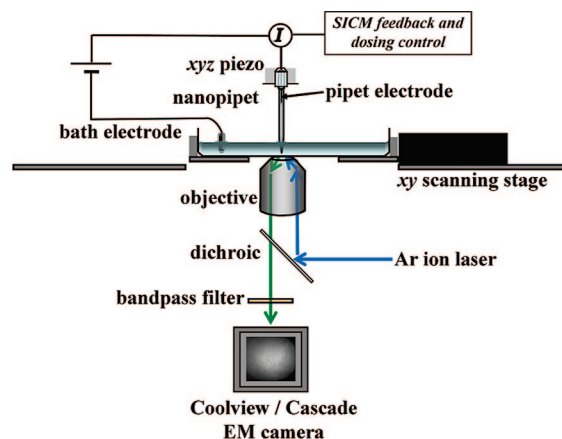


**Figure 1.** Schematic of the apparatus used for localized dosing (see videos V1 and V4 and the related text in the Supporting Information).

cent dyes in the pipet tip in order to map the local concentration of the analyte.<sup>27</sup> All of these experiments used the pipet as a continuous ionic source. In this work, we have extended the application of the nanopipet by using it as a pulsed source, allowing it to act as a “nanosource” to produce a local quantified chemical change at a surface through local voltage-driven delivery of reagents to an area as small as  $1\ \mu\text{m}^2$  with a time response of 10 ms.

We first quantified the chemical change produced at a surface when dosing either  $\text{Na}^+$  or  $\text{OH}^-$  ions from the pipet using total internal reflection fluorescence (TIRF) imaging with CoroNa Green or fluorescein, respectively, as the reporter dye. We characterized the dependence of the concentration change produced on the dosing voltage, the distance of the pipet from the surface, and the pipet size. We also demonstrated that fast local concentration changes (within 10 ms) are possible. We then performed single-cell and single-molecule experiments to demonstrate the applicability of this method. First,  $\text{Na}^+$  ions were dosed in order to alter the speed of the *Escherichia coli* chimeric  $\text{Na}^+$ -driven flagellar motor without flow effects.<sup>28</sup> Second,  $\text{H}^+$  ions were delivered in order to locally acid-melt single molecules of duplex DNA.

## 2. Materials and Methods

**2.1. Nanosource Preparation and Experimental Setup.** The apparatus used in these experiments is shown in Figure 1 and is described in further detail in the Supporting Information and elsewhere.<sup>20,25,26</sup> Briefly, 100 and 320 nm pipets were made from glass capillaries using a laser-actuated pipet puller and mounted on the pipet holder. The SICM instrument used the ion current through the tip as feedback to control the pipet. An argon ion laser illuminated the surface under TIRF microscopy, and the fluorescence was collected by the optics and focused onto an electron-multiplying charge-coupled device (EMCCD) camera. The microscope lamp was used for pipet alignment as well as detection of the beads. The sample was contained in a 50 mm diameter glass-bottom dish (Willco Wells GWST 1000) typically containing 3 mL of electrolyte solution.

For spatial distribution measurements of the nanosource, videos with 20 images were acquired, while for time response measurements, 200 images were taken. Averaging was performed with at least 10 images, but no further image analysis was performed.

- (10) Salaita, K.; Wang, Y. H.; Mirkin, C. A. *Nat. Nanotechnol.* **2007**, *2*, 145–155.
- (11) Piner, R. D.; Zhu, J.; Xu, F.; Hong, S. H.; Mirkin, C. A. *Science* **1999**, *283*, 661–663.
- (12) Rudd, N. C.; Cannan, S.; Bitziou, E.; Ciani, L.; Whitworth, A. L.; Unwin, P. R. *Anal. Chem.* **2005**, *77*, 6205–6217.
- (13) Boldt, F. M.; Heinze, J.; Diez, M.; Petersen, J.; Borsch, M. *Anal. Chem.* **2004**, *76*, 3473–3481.
- (14) Moldovan, N.; Kim, K. H.; Espinosa, H. D. *J. Microelectromech. Syst.* **2006**, *15*, 204–213.
- (15) Cook, P. B.; Werblin, F. S. *J. Neurosci. Methods* **1994**, *14*, 3852–3861.
- (16) Yue, C. Y.; Yaari, Y. *J. Neurophysiol.* **2006**, *95*, 3480–3495.
- (17) Maguire, G.; Lukasiewicz, P.; Werblin, F. *J. Neurosci.* **1989**, *9*, 726–735.
- (18) Maguire, G. *Proc. R. Soc. London* **1999**, *B266*, 987–992.
- (19) Laforge, F. O.; Carpino, J.; Rotenberg, S. A.; Mirkin, M. V. *Proc. Natl. Acad. Sci. U.S.A.* **2007**, *104*, 11895–11900.
- (20) Bruckbauer, A.; Zhou, D. J.; Kang, D. J.; Korchev, Y. E.; Abell, C.; Klenerman, D. *J. Am. Chem. Soc.* **2004**, *126*, 6508–6509.
- (21) Bruckbauer, A.; Zhou, D. J.; Ying, L. M.; Korchev, Y. E.; Abell, C.; Klenerman, D. *J. Am. Chem. Soc.* **2003**, *125*, 9834–9839.
- (22) Hansma, P. K.; Drake, B.; Marti, O.; Gould, S. A. C.; Prater, C. B. *Science* **1989**, *243*, 641–643.
- (23) Korchev, Y. E.; Bashford, C. L.; Milovanovic, M.; Vodyanoy, I.; Lab, M. J. *Biophys. J.* **1997**, *73*, 653–658.
- (24) Korchev, Y. E.; Negulyaev, Y. A.; Edwards, C. R. W.; Vodyanoy, I.; Lab, M. J. *J. Nat. Cell Biol.* **2000**, *2*, 616–619.
- (25) Ying, L. M.; Bruckbauer, A.; Zhou, D. J.; Gorelik, J.; Shevehuk, A.; Lab, M.; Korchev, Y.; Klenerman, D. *Phys. Chem. Chem. Phys.* **2005**, *7*, 2859–2866.
- (26) Bruckbauer, A.; James, P.; Zhou, D. J.; Yoon, J. W.; Excell, D.; Korchev, Y.; Jones, R.; Klenerman, D. *Biophys. J.* **2007**, *93*, 3120–3131.

- (27) Piper, J. D.; Clarke, R. W.; Korchev, Y. E.; Ying, L. M.; Klenerman, D. *J. Am. Chem. Soc.* **2006**, *128*, 16462–16463.
- (28) Sowa, Y.; Rowe, A. D.; Leake, M. C.; Yakushi, T.; Homma, M.; Ishijima, A.; Berry, R. M. *Nature* **2005**, *437*, 916–919.

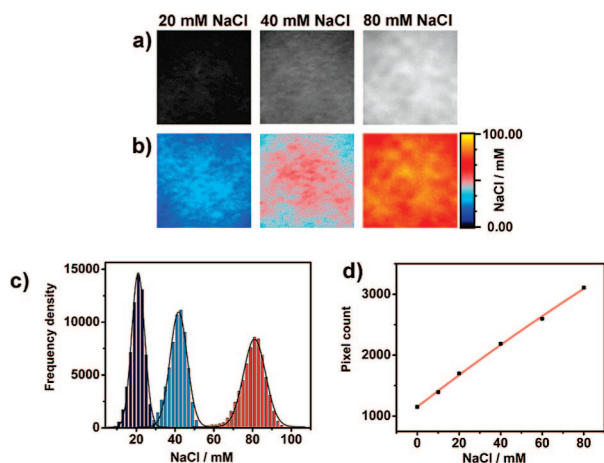


**Figure 2.** Calibration of the fluorescent images relating pixel count to analyte ion concentration, shown here for NaCl: (a) sample TIRF titration images for different sodium concentrations; (b) calibration images converted to sodium concentrations using only the parameters from the titration fit; (c) histograms of the calibration images, where the fwhm defined the accuracy; (d) the overall titration curve.

**2.2. Calibration of  $\text{Na}^+$  Ion Concentration.** For the  $\text{Na}^+$  calibration experiments, 10  $\mu\text{M}$  CoroNa Green and 100 mM KCl were used in the pipet and bath. Quantification of the dosing concentration at the surface was accomplished by recording TIRF images at different analyte concentrations and then relating the pixel intensities to the ion concentrations using the following equation:

$$[\text{Na}^+] = K_d \frac{F - F_{\min}}{F_{\max} - F} \quad (1)$$

where  $F$  is the fluorescent intensity and  $F_{\max}$  and  $F_{\min}$  are the maximum and minimum fluorescent intensities measured at the highest and lowest concentrations of  $\text{Na}^+$  ions, respectively. The values of  $K_d$ ,  $F_{\max}$ , and  $F_{\min}$  were found experimentally from the fit to the titration data. The camera gain and offset were optimized for sensitivity for the concentration range measured.

Each point of the titration was calculated by averaging over a fixed range of  $250 \times 250$  pixels in the center of the TIRF microscopy field. The resulting calibration curves for CoroNa Green with  $\text{Na}^+$  are shown in Figure 2. The illuminated area was displaced laterally at least 5 times, and the standard error of these measurements is shown on the graphs. Individual images had slight variations, although the calculated sodium image histograms were centered on the calibration concentration (Figure 2c). The surface was confirmed to be free of local impurities and have minimal fluorescence surface variation. Measurements of the fwhm of the histograms provided a maximum error of  $\pm 8$  mM for a NaCl concentration range of 0–100 mM, and this error was smaller at lower concentrations. For the range 0–1 M NaCl, the error was  $\pm 15$  mM. Initial experiments demonstrated that at the laser power employed in all of the experiments, 1.1 mW, photobleaching was insignificant for both fluorescein and CoroNa Green (see the Supporting Information).

The time response was measured using several  $10 \times 10$  pixel areas selected near the tip in order to prevent smoothing of the response due to bulk averaging of the data. The response time was defined as the difference of the times at which 10 and 90% of the maximum signal were observed.

**2.3. pH Calibration.** For the pH calibration experiments, 10  $\mu\text{M}$  fluorescein and 100 mM KCl were used in the bath. The calibration experiments were performed both in 100 mM ascorbic acid buffered at pH 5.0 and in MilliQ water in a manner analogous to that for sodium (see Figure S6 in the Supporting Information). A logistic step function measured pixel intensities that corresponded to pH readings of between 5.0 and 7.3 fitted using Origin 7.0. A

MATLAB routine then defined any measured pixel counts below the threshold as pH 5.0 or above it as pH 7.3. The pH could be measured with an accuracy of  $\pm 0.15$ , as deduced from the fwhm of the plotted Gaussians.

**2.4. Measurement of Local Changes Produced by Pipet Dosing.** For the sodium dosing experiments, 10  $\mu\text{M}$  CoroNa Green and 100 mM KCl were used in the pipet and bath. NaCl concentrations of 100 mM or 5 M were used in the pipet along with a magnification of  $60\times$  (i.e., the objective). Control experiments were performed with equal amounts of NaCl in the pipet and bath (first with 100 mM NaCl in both and then with 0 mM in both) in order to verify that none of the observed changes in fluorescence were due to flow effects that occurred on application of voltage to the pipet.

For the pH dosing experiments, 10  $\mu\text{M}$  fluorescein and 100 mM KCl were used in the pipet and bath, and the pipet also contained 1 M KOH; the magnification was  $90\times$  (i.e., the same objective as before, but with an additional  $1.5\times$  magnification). Control experiments to investigate flow effects were also repeated for fluorescein with 0 M KOH in both the pipet and bath and again with 1 M KOH in both the pipet and bath. No artifacts due to flow or applied voltage were observed.

All of the dosing experiments were repeated at least twice with different pipets.

**2.5. Bacterial Flagellar Motor Control.** In *E. coli*, the membrane potential and pH gradient are strongly correlated and difficult to manipulate independently. Hence, in this work we studied chimeric sodium-driven flagellar motors in *E. coli*, which contained rotors from the proton-driven *E. coli* motor and stators combining proteins from the proton-driven *E. coli* and sodium-driven *Vibrio alginolyticus* motors.<sup>28–30</sup> It has been shown that the rotational motor speed is proportional to the sodium motive force (smf) generated by the sodium ion gradient across the membrane.<sup>30</sup> Hence, this was a suitable biological system to exploit the local and quantified changes in sodium concentration available with the nanopipet.

*E. coli* strain YS34 ( $\Delta cheY$ ,  $fliC::Tn10$ ,  $\Delta pilA$ ,  $\Delta motAmotB$ ) with plasmid pYS11 (*fliC* sticky filaments) and a second plasmid pYS13 (*pomA* *ApotB*<sup>7E</sup>) for inducible expression of stator proteins were used in our experiments.<sup>28</sup> Cells were grown in T broth [1% tryptone (Difco, Detroit, MI), 0.5% NaCl] for 5 h at 30  $^\circ\text{C}$  from frozen stock containing the appropriate antibiotics and 20  $\mu\text{M}$  isopropyl- $\beta$ -D-thiogalactopyranoside to induce the stator proteins.

The *E. coli* cells containing the chimeric  $\text{Na}^+$  ion-driven flagellar motor then had the majority of their flagellar filaments sheared off, leaving  $\leq 1$   $\mu\text{m}$  remaining. The cells were fixed on a 50 mm diameter polylysine-coated glass-bottom disk. Polystyrene beads (1  $\mu\text{m}$  diameter) were then tethered to the remaining flagella stubs to enable visualization of the flagellar rotation by bright-field microscopy.<sup>28,30</sup> The dish was filled with motility buffer (10 mM potassium phosphate, pH 7.0) containing varying NaCl concentrations with a constant total ionic strength (i.e.,  $[\text{NaCl}] + [\text{KCl}] = 85$  mM). All of the bacteria dosing experiments were captured at 178 frames per second (fps).

Control experiments were performed with *E. coli* in 85 mM NaCl motility buffer and a nanopipet containing the same buffer. The nanopipet was laterally displaced  $\sim 1$   $\mu\text{m}$  away from the motor and the height varied between 25  $\mu\text{m}$  and 50 nm. No effect due to pipet proximity or dosing voltage was observed (Figure S11 in the Supporting Information).

Sodium ion delivery was performed using a 100 nm diameter nanopipet back-filled with 5 M NaCl in motility buffer. The nanopipet was placed 50 nm from the surface and laterally displaced  $\sim 3$   $\mu\text{m}$  from an *E. coli* cell with a spinning flagellar motor identified by a rotating bead. A voltage of  $-0.2$  V was applied to the

(29) Lo, C. J.; Leake, M. C.; Berry, R. M. *Biophys. J.* **2006**, *90*, 357–365.

(30) Lo, C. J.; Leake, M. C.; Pilizota, T.; Berry, R. M. *Biophys. J.* **2007**, *93*, 294–302.



nanopipet to cause ionic current to flow as a basis for feedback to detect the surface. A typical dosing voltage was  $-6$  V.

**2.6. Single-Molecule DNA Unfolding.** Protonation of the bases in duplex DNA disrupts Watson–Crick base pairing and lowers its melting point. This effect could be locally studied by pulsed dosing of acid with the nanopipet. A 12-mer biotinylated duplex fluorescent resonance energy transfer (FRET) system was designed with Alexa Fluor 488 as the donor on one strand and Atto 647N as the acceptor on the other (see the Supporting Information). In these experiments, a compromise between producing a large enough pH change to ensure unfolding and minimizing the size of the area on the surface where the local pH change occurs had to be made. Hence, on the basis of the pH calibration experiments for this buffer (Figure S10 in the Supporting Information), we chose a voltage of  $+0.15$  V in 10 mM Tris buffer to produce a pH decrease of 2 units in an area of  $\sim 4$   $\mu\text{m}$  diameter. A NaCl concentration of 10 mM was selected through characterization of the unfolding DNA sample (see the Supporting Information). The feedback voltage of  $+0.6$  V provided ionic feedback control and prevented any leakage of acid until the dosing voltage of  $+0.15$  V was selected (the large concentration of acid in the pipet caused a small offset).

Biotinylated DNA duplex molecules (10 nM) were surface-immobilized via a BSA–biotin/streptavidin linkage in 10 mM Tris buffer containing 10 mM NaCl and scanned confocally at a low laser power of 3.9  $\mu\text{W}$  at a wavelength of 488 nm. Repeatable images of the same area were obtained without significant photobleaching on both the donor and acceptor channels (data not shown). Hydrogen ion delivery was performed using a 100 nm diameter nanopipet back-filled with 1 M HCl and 10 mM NaCl. It was not possible to monitor the unfolding process during acid delivery, as the fluorescent properties of the dyes were altered by the acid; therefore, the DNA was monitored once delivery was complete. A  $+0.15$  V pulse of 25–30 s duration was applied to locally unfold the DNA duplex layer.

To demonstrate triggered single-molecule reactions using a nanopipet, we repeated the localized dissociation experiment with a lower surface density. The nanopipet unfolded only a few ( $<20$ ) molecules of duplex DNA, and single molecules were monitored confocally through their individual fluorescence trajectories. Using a 50 pM acceptor concentration, the observation of one-step photobleaching events confirmed that single molecules were present on the surface (see the Supporting Information).

### 3. Results and Discussion

The principle of these experiments was to deliver either  $\text{Na}^+$  or  $\text{OH}^-$  ions from the pipet using voltage-driven delivery in order to produce a local change in the surface  $\text{Na}^+$  concentration or the pH, respectively. After calibration experiments were performed, the fluorescence from CoroNa Green (for  $\text{Na}^+$ ) or fluorescein (for pH) in the bath could be used to measure the changes in local concentration produced by the pipet. This was done using TIRF imaging to probe concentration changes close to the surface, within the evanescent field of 70 nm penetration depth (Figure 1). After the local changes produced by pipet dosing were characterized in detail, two proof-of-concept experiments on single cells and single molecules were performed in order to demonstrate the broad applicability of this method.

**3.1. Sodium Ion Dosing.** Local concentration changes were first characterized by dosing  $\text{Na}^+$  ions from the nanopipet as a function of nanopipet inner diameter, applied voltage, height above the surface, and concentration in the pipet. We focused here on the localized changes in small pipets, defined as pipets having a diameter of either 100 or 320 nm, as this size could produce the most local changes. For example, Figure 3 shows the effects of  $-6$  and  $-0.2$  V dosing voltages for pipets with an inner diameter of 100 nm filled with 5 M NaCl and a bath

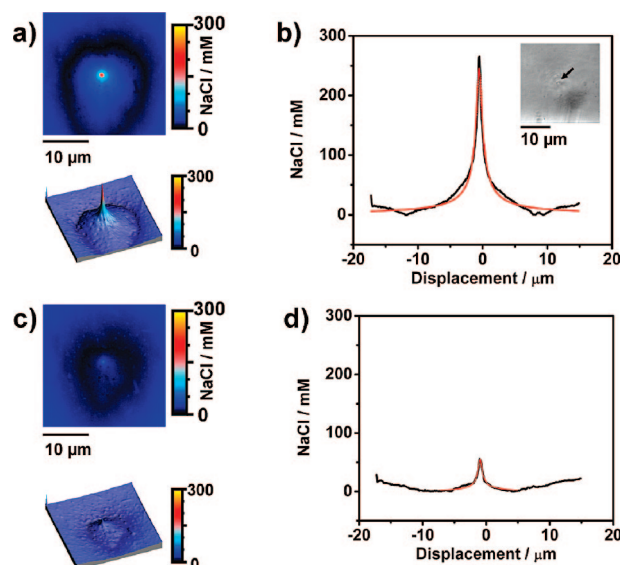


**Figure 3.** Mapping of sodium contours as a function of voltage for a 100 nm diameter pipet loaded with 5 M NaCl ( $n = 3$  pipets): (a) concentration distribution at  $-6$  V; (b) linescan for  $-6$  V dosing concentration fitted to steady-state diffusion from a hemispherical pore (inset: 100 nm pipet on the surface); (c) the concentration distribution at  $-0.2$  V; (d) linescan for  $-0.2$  V fitted to steady-state diffusion. These conditions were used for dosing the bacteria (Section 3.4 in the text).

containing 100 mM KCl. These were the conditions used for the bacterial-motor sodium dosing experiment discussed in Section 3.4.

The sodium nanosource was modeled in terms of steady-state diffusion from a hemispherical pore of fixed diameter (corresponding to the nanopipet) with variable concentration and distance (see the Supporting Information). The sodium distribution resembled that from a pore that was slightly higher than the pipet control radius with a lower effective concentration. Hence, the 100 nm pipets behaved as if they were slightly depleted in the tip region by the bath solution.<sup>31</sup>

We also explored the effects of pipet size, distance, and applied voltage. When the pipets containing 100 mM NaCl were ionically balanced with 100 mM KCl in the bath, only the 2  $\mu\text{m}$  pipets produced this  $\text{Na}^+$  ion concentration at the surface, while the 100 nm pipets produced a local concentration of 30 mM. In general, we found that the smaller pipets gave a more localized source. Additional control of the distribution was also found to be possible by variation of the dosing voltage and pipet height. Representative data are shown in Figure 4 for a 320 nm diameter pipet, as this provides the clearest dependence on voltage and height within the resolution of the instrument.

Local depletion of sodium was also demonstrated by dosing 100 mM KCl. Here the effect was largest with the largest pipet diameter used (2  $\mu\text{m}$ ) (see Figure S2 in the Supporting Information).

**3.2. Time Response.** The 100 nm nanopipet provided the nanosource with the fastest time response as well as highly targeted dosing for sodium. The 100 nm nanopipet loaded with 5 M NaCl and at a dosing voltage of 10 V gave an optimal rise time around the  $\sim 1$   $\mu\text{m}^2$  pipet tip area of  $28.8 \pm 2.5$  ms between 10% and 90% of the signal measured at 278 fps. The decay time was  $10.8 \pm 2.5$  ms from 90% to 10% of the signal. A

(31) Clarke, R. W.; Piper, J. D.; Ying, L. M.; Klenerman, D. *Phys. Rev. Lett.* **2007**, *98*, 198102.

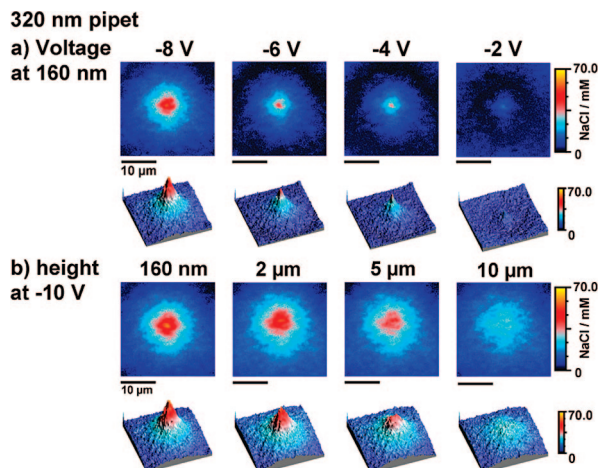


**Figure 4.** Variation of the ionic dosing profile ( $n = 4$  pipets) for a 320 nm diameter, 100 mM NaCl pipet as a function of (a) voltage at a height of 160 nm and (b) height at a dosing voltage of  $-10$  V.

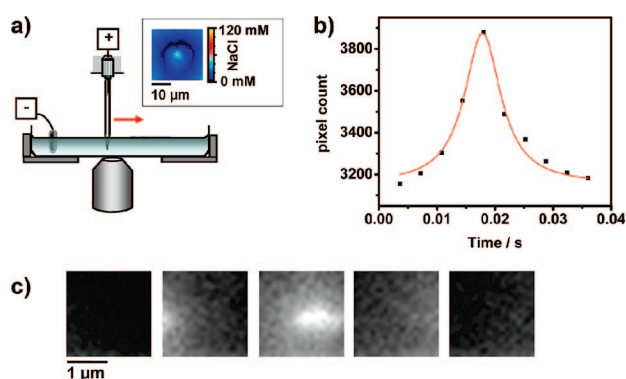


**Figure 5.** Fast delivery using the nanosource ( $n = 2$  pipets): (a) schematic showing translation of the pipet across the illumination area at  $\sim 200 \mu\text{m s}^{-1}$  (inset: sodium dosing profile at  $-0.6$  V); (b) fluorescence response measured at 3.6 ms exposure per frame; (c) five consecutive frames showing the horizontal translation of the nanosource used to find the response measured in (b).

visualization of the fast time response for the 5 M dosing processed frame by frame is shown in Figure S4 in the Supporting Information. For a lateral displacement of a few microns away from the tip, the response was  $\sim 200$  ms measured at 36 fps (see Section 3.4). It was generally observed that the steady-state dosing profile was extremely stable for over 10 min and depended only upon nanopipet drift (which was minimal).

The time response of the nanosource could be increased considerably by constantly dosing and moving the piezoelectric scanner in the pipet mount. When the pipet was translated across the detection region, the fwhm change was  $\sim 10$  ms measured at 278 fps (Figure 5). This is ideally used for flat samples in order to prevent lateral crashing of the pipet. For speed, the pipet was lowered under control at  $-0.6$  V and then moved quickly across the sample at  $\sim 200 \mu\text{m s}^{-1}$ . The NaCl concentration changed by  $\sim 100$  mM during these measurements (Figure 5a). To obtain the best signal-to-noise ratio, we used a laser power of 30 mW. For this fast response, varying the detection area (25 or 400 pixels) did not change the measured response.

**3.3. KOH Dosing.** To image local pH changes, similar investigations were performed with the dosing of  $\text{OH}^-$  ions into fluorescein. As before, the most local changes were achieved

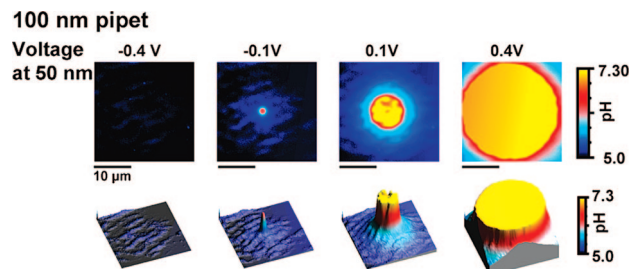


**Figure 6.** Local variation of the pH achieved as a function of voltage when dosing 1 M KOH ( $n = 3$  pipets) under the optimum conditions of highest buffer concentration (100 mM ascorbic acid at pH 5.0) and smallest pipet diameter (100 nm).

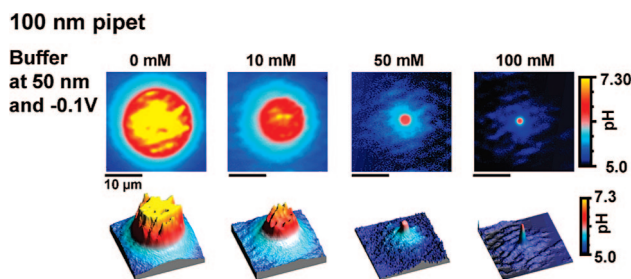


**Figure 7.** Visualization of the effect of buffer concentration for a pH nanosource with  $-0.1$  V applied to dose 1 M KOH ( $n = 2$  pipets). Increasing the buffer concentration led to a more localized, more stable nanosource.

with the smallest diameter (100 nm) pipet (see Figure S7 in the Supporting Information).

Dosing of 1 M KOH from the 100 nm nanopipet at  $-0.1$  V with 100 mM buffer was fitted to steady-state diffusion from a cylindrical electrode of radius 300 nm, reflecting the buffering in solution. Precise control of the local pH nanosource as a function of voltage was possible only for the 100 nm pipet. The localized dosing was best for a high buffer concentration of 100 mM and low voltages ( $< 0.4$  V), as shown in Figure 6.

The effect of buffering could also be clearly seen in these experiments (Figure 7). Increasing the buffer concentration provided a more localized, more stable pH source. The MilliQ water was itself slightly buffered with carbonic acid and carbon dioxide from the air ( $\sim \text{pH } 5.65$ ), so some localization was achieved even without buffer.

Within  $\sim 1 \mu\text{m}^2$  of the tip region, the 100 nm nanopipet dosed to the measured pH within 80 ms per frame and relaxed within  $120 \pm 60$  ms. Addition of buffer reduced the dosing area (Figure 7), with similar dosing and relaxation times. Again, for buffer concentrations of 10 mM or greater, the steady-state pH dosing distribution was observed to be extremely stable for  $> 10$  min.

**3.4. Controlling the Chimeric Flagellar Motor in *E. coli*.** The speed of the sodium-sensitive *E. coli* chimeric flagellar motor increases with increasing sodium concentration. Therefore, we used quantified local sodium concentration changes produced by the nanopipet to alter the motor speed, which was measured by recording the position of a bead attached to the flagellar motor, as shown in Figure 8.

Pipet proximity and applied voltage effects are insignificant, as evidenced by the fact that control experiments with 85 mM NaCl in both the pipet and bath showed no alteration of the speed of the *E. coli* motor (see the Supporting Information). The motor responded to “slow” sodium dosing (defined as alternating between typically 30–50 s at  $-0.2$  V and 30–50 s



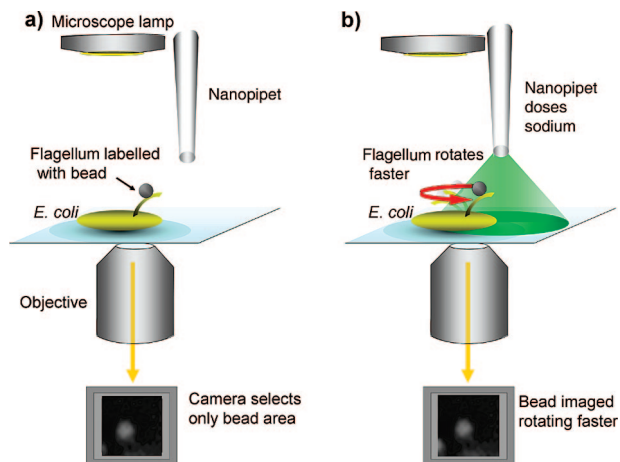


**Figure 8.** Schematic diagram (not to scale) of the experimental setup for triggering of a single *E. coli* sodium-driven chimeric flagellar motor (a) before and (b) while the nanopipet doses sodium with an applied voltage and causes the flagellum to rotate faster. Detection is via a camera that images the bead illuminated by the microscope lamp.

at  $-6$  V) in a manner similar to that previously observed in flow-cell chamber experiments.<sup>28</sup>

The dosing sodium concentration was quantitatively determined by the distance from the nanosource and the voltage applied, using the NaCl calibration described earlier. Therefore, the  $\text{Na}^+$  concentrations shown in Figure 9 correspond to the actual, calibrated local concentrations from the control experiments portrayed in Figure 3. It has been reported that the stators become inactive under low-sodium conditions and resurrect when sodium is reintroduced.<sup>28,32</sup> At lower dosing concentrations, reversible inactivation of stator units and subsequent recovery of the motor rotation was visible (Figure 9a).

The motors also responded to a larger rate of sodium concentration pulses. Figure 9b shows a raw speed trace when 5 mM (i.e., “low”) sodium for 2 s followed by 36 mM (i.e., “high”) sodium for 4 s was applied (see video V6 in the Supporting Information). The power spectrum of the motor speed had a peak at 0.166 Hz corresponding to the 6 s dosing period (data not shown).

For this shorter dosing (i.e., 1–2 s of low sodium and 4–10 s of high sodium), the motor’s rotational speed has a clear response (Figure 9b,c). There was typically a  $\sim 200$  ms delay in the bacteria’s response to sodium dosing control from the pipet. This correlates well with the nanosource at  $-6$  V: at a displacement of 3–5  $\mu\text{m}$ , the measured time response of the nanosource was 130–250 ms. The time for the nanosource to relax to bath equilibrium at this distance was 180–240 ms, while the decrease in motor speed took significantly longer ( $\sim 1$  s). Hence, there appears to be a delay in the bacteria’s response to a sudden decrease in sodium concentration. The sodium ions are driven by the smf due to the membrane potential and sodium gradient across the membrane. When the motor was loaded with a 1  $\mu\text{m}$  bead (forcing the motor to drive a large load), the motor speed was proportional to the total sodium motive force.<sup>30</sup> The noninstantaneous speed decrease is probably due to periplasmic sodium buffering. Previous measurements have been able to globally decrease the sodium concentration only within 5 s.<sup>28</sup>

The noise in these experiments is due to the combined effect of smf variations and instrumental noise. From previous high-

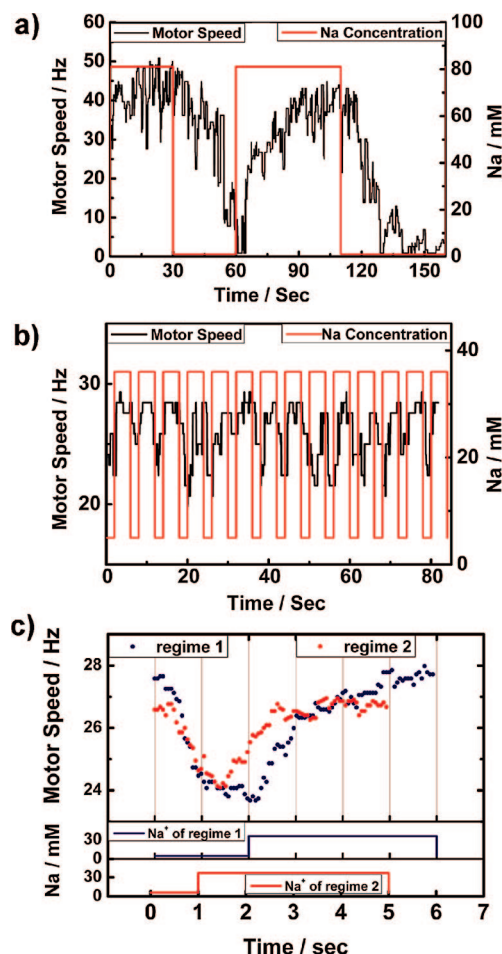


**Figure 9.** Control of sodium-driven chimeric flagellar motor rotation by quantitative pulsing from a nanopipet of (a) 81 mM  $\text{Na}^+$  for 30 s followed by 1 mM  $\text{Na}^+$  for 30 s and then 81 mM  $\text{Na}^+$  for 50 s followed by 1 mM  $\text{Na}^+$  for 50 s and (b) repeated cycles of 5 mM  $\text{Na}^+$  for 2 s followed by 36 mM  $\text{Na}^+$  for 4 s. (c) The averaged speed responses of the same motor to different dosing conditions: regime 1 is the averaged data for the trace in (b), while regime 2 is the averaged data for the same motor for cycles of 5 mM  $\text{Na}^+$  for 1 s followed by 36 mM  $\text{Na}^+$  for 4 s.

resolution bacteria flagellar measurements,<sup>30</sup> noise typically contributes a deviation of  $\sim 10\%$  of the speed. In the pipet dosing experiments, the video rate is slower and the contrast is less, so there is greater noise in the calculation of position. Additional uncertainty occurs as the sodium concentration changes because the cells must continually adjust their energetics in response.

We have demonstrated fast, local control of the bacterial flagellar motor on a time scale of 1 s (no measurable response of the motor was observed at faster pulsing rates). In all, we recorded results for nine separate motors. The number of torque-generating stators in the bacterial flagellar motor is sensitive to the free energy produced by the ion gradient across the membrane. Stators have been shown to be in dynamic exchange between torque-generating units in a motor and others circulating in the cell, demonstrating resurrection when the sodium concentration is increased (Figure 9a).<sup>30</sup> Hence, the nanopipet provides a novel method for studying the dynamic interactions of individual cell membrane systems, as demonstrated here with the flagellar motor.

**3.5. Triggering of Individual Molecules: DNA Melting.** The pipet can also be used for localized melting of individual DNA molecules by delivery of  $\text{H}^+$  ions, as shown in Figure 10. The

(32) Reid, S. W.; Leake, M. C.; Chandler, J. H.; Lo, C. J.; Armitage, J. P.; Berry, R. M. *Proc. Natl. Acad. Sci. U.S.A.* **2006**, *103*, 8066–8071.

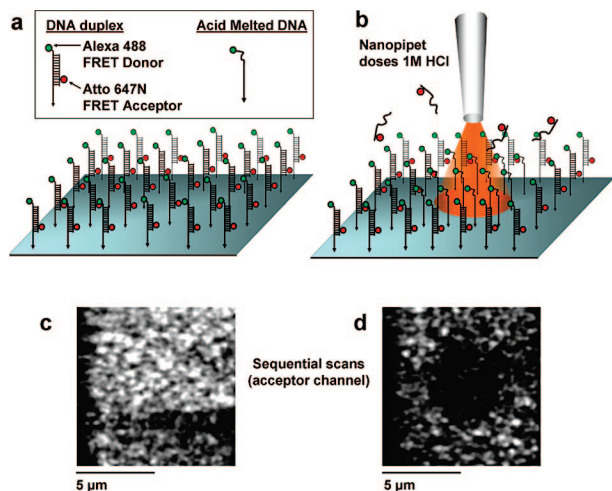


**Figure 10.** (a) Schematic representation of the carpet of the biotinylated duplex DNA FRET system with the FRET donor on the biotinylated strand and the FRET acceptor on the complementary 12-mer strand. When the DNA dissociates, only the donor is detected. (b) Localized melting as 1 M HCl is dosed from a nanopipet brought close to the surface ( $n = 6$ ). (c, d) Corresponding fluorescence images ( $100 \mu\text{m}^2$  sequential scans) at low laser power in the acceptor channel. In (d), the hole formed when locally dosed acid from the pipet melted away the complementary 12-mer acceptor strand is visible in the center. The pH here was locally decreased to pH 5.0 for 25 s (see video V4 and related text in the Supporting Information).

pipet was positioned over the DNA with no leakage of acid until the delivery pulse was activated. We then locally dosed a 10 nM carpet of surface-immobilized biotinylated duplex DNA containing a FRET donor and a FRET acceptor on complementary strands. Locally dosing 1 M HCl from a 100 nm nanopipet for 25–30 s caused the DNA strand with the acceptor to dissociate from the biotinylated DNA strand with the donor, resulting in a corresponding drop in FRET acceptor intensity. Following  $\text{H}^+$  ion delivery from the nanopipet, the DNA duplex layer had a dark hole in the acceptor channel image (Figure 10d). A hole with a diameter of  $\sim 4 \mu\text{m}$  suggests that this was the effective area on the surface where the pH change was at least 2 units.

The hole visible in Figure 10 is larger than the most localized dosing shown in Figure 7 because the DNA Tris buffer concentration was only 10 mM. Hence, the bulk unfolding was more comparable to the calibration experiments done in 10 mM buffer (see Figure S10 in the Supporting Information). To demonstrate triggered single-molecule reactions using a nanopipet, we repeated the localized dissociation experiment with single molecules of duplex DNA and monitored their individual fluorescence trajectories in the confocal volume. At an acceptor concentration of 50 pM, the observation of one-step photobleaching events confirmed that single molecules were present on the surface (see the Supporting Information).

Single molecules were detected in the acceptor channel and locally unfolded (Figure 11) or observed for a similar time frame as a control. Representative single-molecule traces from DNA unfolding and control experiments are shown in Figure 11b. In the control experiments, the acceptor was still detectable after 30 s, whereas using the pipet to locally dose acid reduced the acceptor's signal to the background level. The control experiments ruled out contributions to the disappearance of the acceptor fluorescence from artifacts such as photobleaching or drift. A total of 10 molecules were unfolded by local dosing of

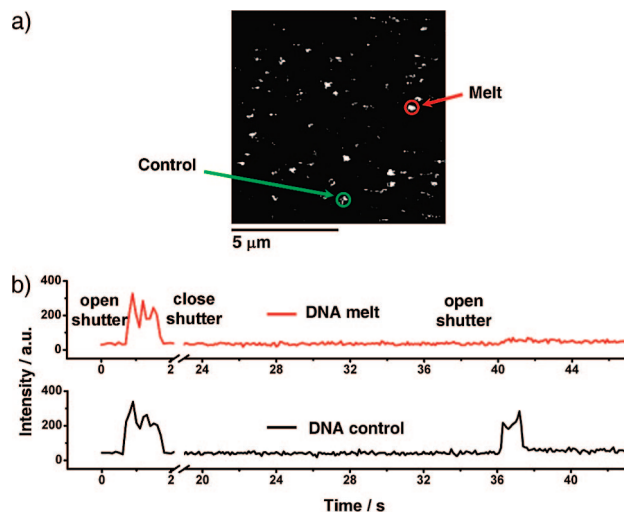


**Figure 11.** Triggered single-molecule dissociation. The confocal spot was focused on a single molecule already imaged on a  $100 \mu\text{m}^2$  scan. The shutter was opened briefly to check for the presence of a molecule and then closed. The 100 nm diameter nanopipet was brought into control with the surface at +0.6 V and then started dosing at +0.15 V. After dosing was complete, the shutter was again opened to see whether the acceptor strand had melted. (a) Representative image with molecules selected for melting and control. (b) Representative traces of single DNA molecule melting (red line,  $n = 10$ ) and the control monitored for a similar time frame (black line,  $n = 10$ ), showing single-step photobleaching.

acid and another 10 observed for a similar time period as controls by monitoring their trajectories with the confocal spot. In addition, two molecules did not unfold despite dosing with acid, and two others did disappear between the first and second openings of the shutter (see the Supporting Information for experimental details). This DNA unfolding experiment reveals the advantage of nanopipet-triggered chemical reactions, as reagents can be rapidly and locally delivered to a region on the surface with a diameter of  $< 5 \mu\text{m}$  and applied for at least 1 min.

#### 4. Conclusion

We have shown that a nanopipet can dose localized, controlled changes in reagent concentration at a surface that can be used to initiate a single-molecule reaction or control a molecular motor's speed of rotation. These changes are possible within a 10 ms time frame, and further optimization should enable a time resolution of  $\sim 1$  ms. We have demonstrated triggered single-molecule unfolding using DNA. Using this novel tool, we have also varied the sodium concentration in a new time regime in order to initially probe periplasmic buffering of the sodium motor in an *E. coli* chimera.

Our approach is versatile and allows local and repeatable delivery (or depletion) of any water-soluble reagent or mixture of reagents from the pipet in physiological buffer without the need for any reagents in the solution. For example, targeted delivery of chemical denaturants such as urea or guanidinium chloride as well as of functional biological molecules is possible. Furthermore, since the pipet can be scanned over a surface without contact using ion-conductance distance feedback, it becomes feasible to map the chemical reactivities of surfaces under aqueous conditions and relate this to surface topography. This could be used on many surface types, including metals and polymers as well as living cells.



**Acknowledgment.** This work was funded by the BBSRC. We thank Ji Won Yoon for writing the MATLAB code to analyze the pH dosing. We also thank Dr. Dejian Zhou for help constructing the confocal microscope and Dr. Andreas Bruckbauer for assistance with the TIRF imaging.

**Supporting Information Available:** Apparatus description and further nanosource characterization for NaCl and KOH dosing,

bacterial flagellar motor controls together with detailed experimental and sample characterization for DNA melting, and sample dosing videos. This material is available free of charge via the Internet at <http://pubs.acs.org>.

JA8022253